

**Very long baseline interferometry observations of the high-redshift blazar candidate  
J0141–5427**

Gabanyi, K.E.; Belladitta, S. ; Frey, S.; Orosz, G. ; Gurvits, L.; Rozgonyi, Krisztina; An, T. ; Cao, H; Paragi, Z; Perger, Krisztina

**DOI**

[10.1017/pasa.2023.2](https://doi.org/10.1017/pasa.2023.2)

**Publication date**

2023

**Document Version**

Final published version

**Published in**

Publications of the Astronomical Society of Australia

**Citation (APA)**

Gabanyi, K. E., Belladitta, S., Frey, S., Orosz, G., Gurvits, L., Rozgonyi, K., An, T., Cao, H., Paragi, Z., & Perger, K. (2023). Very long baseline interferometry observations of the high-redshift blazar candidate J0141–5427. *Publications of the Astronomical Society of Australia*, 40, Article e004. <https://doi.org/10.1017/pasa.2023.2>

**Important note**

To cite this publication, please use the final published version (if applicable).  
Please check the document version above.

**Copyright**




Other than for strictly personal use, it is not permitted to download, forward or distribute the text or part of it, without the consent of the author(s) and/or copyright holder(s), unless the work is under an open content license such as Creative Commons.

**Takedown policy**

Please contact us and provide details if you believe this document breaches copyrights.  
We will remove access to the work immediately and investigate your claim.

## Research Article

# Very long baseline interferometry observations of the high-redshift blazar candidate J0141–5427

K. É. Gabányi<sup>1,2,3</sup> , S. Belladitta<sup>4,5,6</sup>, S. Frey<sup>2,7,8</sup> , G. Orosz<sup>9,10</sup>, L. I. Gurvits<sup>9,11,12</sup>, K. Rozgonyi<sup>13,14,15</sup>, T. An<sup>16,17</sup>, H. Cao<sup>18</sup>, Z. Paragi<sup>9</sup> and K. Perger<sup>1,2,7</sup> 

<sup>1</sup>Department of Astronomy, Institute of Physics and Astronomy, ELTE Eötvös Loránd University, Pázmány Péter sétány 1/A, H-1117 Budapest, Hungary, <sup>2</sup>Konkoly Observatory, ELKH Research Centre for Astronomy and Earth Sciences, Konkoly Thege Miklós út 15-17, H-1121 Budapest, Hungary, <sup>3</sup>ELKH-ELTE Extragalactic Astrophysics Research Group, ELTE Eötvös Loránd University, Pázmány Péter sétány 1/A, H-1117 Budapest, Hungary, <sup>4</sup>INAF, Osservatorio Astronomico di Brera, Via Brera 28, 20121 Milano, Italy, <sup>5</sup>DISAT, Università degli Studi dell'Insubria, Via Valleggio 11, 22100 Como, Italy, <sup>6</sup>Max-Planck-Institute for Astronomy, Königstuhl 17, 69117 Heidelberg, Germany, <sup>7</sup>CSFK, MTA Centre of Excellence, Konkoly Thege Miklós út 15-17, H-1121 Budapest, Hungary, <sup>8</sup>Institute of Physics and Astronomy, ELTE Eötvös Loránd University, Pázmány Péter sétány 1/A, H-1117 Budapest, Hungary, <sup>9</sup>Joint Institute for VLBI ERIC, Oude Hoogeveensedijk 4, 7991 PD Dwingeloo, The Netherlands, <sup>10</sup>School of Natural Sciences, University of Tasmania, Private Bag 37, Hobart, Tasmania 7001, Australia, <sup>11</sup>Faculty of Aerospace Engineering, Delft University of Technology, Kluyverweg 1, 2629 HS, Delft, The Netherlands, <sup>12</sup>CSIRO Astronomy and Space Science, PO Box 76, Epping, NSW 1710, Australia, <sup>13</sup>University Observatory, Faculty of Physics, Ludwig-Maximilians-Universität, Scheinerstr. 1, 81679 Munich, Germany, <sup>14</sup>International Centre for Radio Astronomy Research, The University of Western Australia, Crawley, WA 6009, Australia, <sup>15</sup>Australian Research Council, Centre of Excellence for All-Sky Astrophysics in 3 Dimensions (ASTRO 3D), Canberra, ACT 2611, Australia, <sup>16</sup>Shanghai Astronomical Observatory, CAS, Nandan Road 80, Shanghai 200030, PR China, <sup>17</sup>Peng Cheng Laboratory, Shenzhen 518066, PR China and <sup>18</sup>School of Physics and Electronic Information, Huanggang Normal University, 146 Xingang 2nd Road, Huanggang, Hubei 438000, PR China

## Abstract

Active galactic nuclei (AGN) have been observed as far as redshift  $z \sim 7$ . They are crucial in investigating the early Universe as well as the growth of supermassive black holes at their centres. Radio-loud AGN with their jets seen at a small viewing angle are called blazars and show relativistic boosting of their emission. Thus, their apparently brighter jets are easier to detect in the high-redshift Universe. DES J014132.4–542749.9 is a radio-luminous but X-ray weak blazar candidate at  $z = 5$ . We conducted high-resolution radio interferometric observations of this source with the Australian Long Baseline Array at 1.7 and 8.5 GHz. A single, compact radio-emitting feature was detected at both frequencies with a flat radio spectrum. We derived the milliarcsecond-level accurate position of the object. The frequency dependence of its brightness temperature is similar to that of blazar sources observed at lower redshifts. Based on our observations, we can confirm its blazar nature. We compared its radio properties with those of two other similarly X-ray-weak and radio-bright AGN, and found that they show very different relativistic boosting characteristics.

**Keywords:** active galactic nuclei – very long baseline interferometry – galaxies: high-redshift

(Received 23 September 2022; revised 6 January 2023; accepted 11 January 2023)

## 1. Introduction

Active galactic nuclei (AGN) are the most luminous persistent astronomical objects, and they are invaluable probes for investigating the high-redshift Universe. Roughly ten per cent of AGN are radio-loud, jetted sources (e.g., Ivezić et al. 2002). In them, the radio emission originates from the synchrotron emission of the jets. When the jets are seen at a small angles to the line of sight, for example,  $\lesssim 10^\circ$  (Urry & Padovani 1995), relativistic beaming causes significant flux density enhancement of the advancing jet. Thus, these beamed sources called blazars can be preferentially detected even at high redshifts ( $z \gtrsim 4$ ) in radio bands.

Blazars can be identified using high-resolution very long baseline interferometry (VLBI) radio observations. They are characterised by a bright feature that is compact at milliarcsec (mas)

scale, the jet base, which usually has a flat radio spectrum at GHz frequencies (e.g., Hovatta et al. 2014). The apparent brightness temperature of this dominant component exceeds the equipartition limit,  $T_B^{\text{eq}} \approx 5 \times 10^{10}$  K (Readhead 1994), and sometimes even the inverse Compton limit ( $\sim 10^{12}$  K, Kellermann & Pauliny-Toth 1969), indicating the potential prevalence of relativistic beaming. Also, apparent superluminal motion of components can often be observed in blazar jets. However, in the case of high-redshift sources, the steep-spectrum jet components are harder to detect, because the observed frequencies correspond to  $(1+z)$  times higher emitted frequencies in the source's rest frame, thus the extended regions of jets are often undetectably faint (Gurvits, Frey, & Paragi 2015).

Blazars can also be classified via their broad-band spectral energy distribution (SED) featuring non-thermal emission over the electromagnetic spectrum and exhibiting relativistic beaming effect (e.g., Massaro et al. 2009).

Belladitta et al. (2019) reported the discovery of DES J014132.4–542749.9 (hereafter J0141–5427), a radio-bright but X-ray-weak AGN at  $z = 5.00 \pm 0.01$ . The source, according to

**Corresponding author:** K. É. Gabányi, Email: [kgabanyi@astro.elte.hu](mailto:kgabanyi@astro.elte.hu)

**Cite this article:** Gabányi KÉ, Belladitta S, Frey S, Orosz G, Gurvits LI, Rozgonyi K, An T, Cao H, Paragi Z and Perger K. (2023) Very long baseline interferometry observations of the high-redshift blazar candidate J0141–5427. *Publications of the Astronomical Society of Australia* 40, e004, 1–7. <https://doi.org/10.1017/pasa.2023.2>

archival data and newly obtained X-ray observations of the authors, is an order of magnitude fainter in X-rays than other blazars with similar radio luminosities. Belladitta *et al.* (2019) showed that the SED of J0141–5427 can be best described with a relativistically beamed blazar SED if a very high magnetic field strength of  $\sim 9$  G is assumed.

We initiated VLBI observations of J0141–5427 with the Australian Long Baseline Array (LBA) at 1.7 and 8.5 GHz to ascertain its blazar nature.

Hereafter, we use the flat  $\Lambda$ CDM cosmological model with parameters of  $H_0 = 70 \text{ km s}^{-1} \text{ Mpc}^{-1}$ ,  $\Omega_m = 0.27$ , and  $\Omega_\Lambda = 0.73$ . At the redshift of J0141–5427, 1 mas angular size corresponds to a projected linear length of  $\sim 6.5$  pc, and the luminosity distance of the object is  $D_L = 48273.2$  Mpc (Wright 2006).

## 2. Observations and data reduction

Observations of J0141–5427 with the LBA were conducted in 2020, under the project code v591 (PI: K. É. Gabányi) in phase-referenced mode (Beasley & Conway 1995). In this observing mode, the pointing directions of the telescopes change regularly between the target source and a nearby phase-reference calibrator within the atmospheric coherence time permitted by the radio propagation media. The delay, and delay rate solutions can be then transferred (interpolated) from the calibrator to the target source. The nodding cycles in both the 1.7 and 8.5 GHz observations were 5 min long, with 3.5 min spent on the target and 1.5 min on the calibrator. The phase-reference calibrator was ICRF J015649.7–543948 in both experiments. Additional calibrator sources were also observed to facilitate amplitude calibration, and to monitor the stability of the array.

The 1.7 GHz observation took place on 2020 June 26 and 27, the participating antennas were Ceduna (CD), Hobart (HO), Mopra (MP), Parkes (PA), the tied array of the Australia Telescope Compact Array (ATCA) in Australia, and Hartebeesthoek (HH) in South Africa. The observation lasted for 10 h, the on-target time was 4.5 h. The 8.5 GHz observation took place on 2020 July 14, with the following participating antennas: CD, HO, MP, PA, Katherine (KE), Yarragadee (YG), the tied array of ATCA in Australia, the 12-m Warkworth antenna (WW) in New Zealand, and HH in South Africa. The observation lasted for 10.25 h, with an on-target time of 4.9 h. In both observations, the total bandwidth of 128 MHz was divided into 8 intermediate frequency bands (IF) of 32 channels each. The correlator integration time was set to 2 s. The correlation was done at the Pawsey Supercomputing Centre in Perth, on a DiFX software correlator (Deller *et al.* 2011). The longest baselines of the arrays (providing the finest angular resolution) were those to HH. At 8.5 GHz, HH could only participate in the last 18 min of the observation.

Data reduction was done using the National Radio Astronomy Observatory (NRAO) Astronomical Image Processing System (AIPS, Greisen 1990) following standard procedures of ionospheric and parallactic angle corrections, manual phase calibrations and fringe-fitting of the calibrator sources, and following the LBA guide on amplitude calibration.<sup>a</sup> The necessary files for amplitude calibration were created from the system temperature measurements and gain curves provided by the participating stations or system equivalent flux densities listed in the LBA

amplitude calibration user's guide. In the absence of system temperature measurements (at the antennas CD and HO at 1.7 GHz and HO, KE, and WW at 8.5 GHz), nominal system temperature values were used.

The fringe-fitting was performed for all calibrator sources. Solutions were found for  $\sim 86\%$  and  $\gtrsim 98\%$  of the data at 1.7 and 8.5 GHz, respectively.

At the AT, MP, and PA antennas, wider filters were used, resulting in clearly lower amplitude values in the channel-averaged data at those IFs corresponding to the edges of the bands (IFs 1, 4, 5, 8) compared to the ones at the middle (IFs 2, 3, 6, 7). Therefore, the edge IFs were scaled up by a constant factor of 1.169 to bring them closer to the values measured in the middle of the band at these antennas in the case of 1.7-GHz observation, before channel averaging. At the 8.5-GHz observation, instead of such scaling, we flagged the first 10 channels for IFs 1 and 5 and the last 10 channels for IFs 4 and 8, for the three antennas using wider filters (AT, MP, and PA).

After the fringe-fitting performed on the calibrator sources, and the application of the above described amplitude scaling for the 1.7-GHz amplitudes, the channel-averaged data of the calibrator sources were imported into the Caltech DIFMAP package (Shepherd 1997) for hybrid mapping. The hybrid-mapping procedure involves subsequent steps of CLEANing (Högbom 1974) and phase self-calibration of the data. As the last step, amplitude self-calibration was done. The gain correction factors obtained for different calibrator sources were in good agreement for the same antennas and IFs. The flux density values of the phase-reference calibrator obtained this way at both frequencies were in good agreement with the ones measured by the ATCA closest in time and at similar frequencies according to the ATCA Calibrator Database<sup>b</sup> with the VLBI-measured flux densities  $\sim 15\%$  and  $\sim 3\%$  lower than the ones measured by ATCA at 1.7 GHz and at 8.5 GHz, respectively. The difference is most probably caused by resolution effect, the LBA observations resolved out the large-scale emission detected by ATCA. Thus, we accepted the gain correction factors obtained in DIFMAP for the phase-reference calibrator, and we adjusted the antenna gains accordingly in AIPS to further improve the amplitude calibration.

To improve the delay and rate solutions, the phase-reference calibrator was fringe-fitted again using the CLEAN component model of its brightness distribution derived from the hybrid mapping, to take the source structure into account. The obtained solutions were applied to the phase-reference calibrator as well as to the target source, and subsequently both were imaged in DIFMAP.

In the case of the phase-reference calibrator, the amplitude self-calibration performed after this second hybrid mapping showed that the gain correction factors were mostly  $\lesssim 10\%$  for the 1.7-GHz data and mostly  $\lesssim 5\%$  for the 8.5-GHz data, except for single IFs of AT and CD, and a few discrepant IFs of YG. Additionally, it seemed that amplitude self-calibration of HH was not constrained at 1.7-GHz, and it could not correct the amplitudes. Thus, we conservatively assume the amplitude calibration of these LBA data is reliable at 10% level.

Due to an unfortunate typing mistake made by the PI at the time of scheduling, the observations and subsequent correlations were done at a target source position with  $4''$  offset in declination

<sup>a</sup><https://www.atnf.csiro.au/vlbi/dokuwiki/doku.php/lbaops/lbcalibrationnotes> (accessed 2022.09.06).

<sup>b</sup>[https://www.narrabri.atnf.csiro.au/calibrators/calibrator\\_database.html](https://www.narrabri.atnf.csiro.au/calibrators/calibrator_database.html) (accessed 2022.09.06).

from the previously known position. A significant offset from the phase centre may cause reduction of the peak intensity and distortion of the obtained image through bandwidth smearing and time-average smearing effects (Bridle & Schwab 1999).

The bandwidth smearing effect would have been substantial (intensity reduction of a point source by  $\sim 80 - 90\%$ ) if the data were averaged over all the channels within an IF (Bridle & Schwab 1999; Wrobel 1995). Therefore, the hybrid mapping of the target source was performed on the unaveraged data. We disregarded the first and last 5 channels of all 8 IFs to account for bandpass effects.

At both frequencies, time averaging was done for 2 s at the correlator. However, because of the different resolutions, time-average smearing affects the two data sets differently. At 1.7 GHz, this effect is negligible, the peak intensity reduction of a point source is less than 1% at 4'' from the pointing centre. At 8.5 GHz, if calculated for the highest achievable resolution obtained with the longest baseline, between HH and YG, time-average smearing would cause an average peak intensity reduction of a point source by 15%. Excluding the baselines to HH, the average amplitude reduction of a point source is  $\sim 5\%$  at 4'' distance. Since HH could only participate in the last 18 min of the 8.5 GHz observation, we excluded the data on the baselines to HH. Therefore the effects of the unintentional pointing offset introduced in the target source position could be mitigated satisfactorily.

The target source J0141-5427 turned out to be bright enough for attempting a direct fringe-fitting. Before that, the visibility data set was shifted by 4'' in declination direction to its a priori known correct position using the task CLCOR in AIPS. At 1.7 GHz, fringes with a signal-to-noise level exceeding  $6\sigma$  were found for 69% of data, including the longest baselines to HH. We continued imaging both the fringe-fitted and the phase-referenced 1.7-GHz data of the target, and the results were in good agreement. The peak intensity was less by  $\sim 10 \text{ mJy beam}^{-1}$  ( $\sim 13\%$ ) in the phase-referenced image compared to the one obtained after fringe-fitting the data due to the coherence loss (Martí-Vidal et al. 2010). At 8.5 GHz, at the same signal-to-noise level, fringes were found for only 24% of data, and no fringes were found on the baselines to HH. Therefore, we did not use the fringe-fitted data of the target for the higher frequency observation.

At both frequencies, phase self-calibration and amplitude self-calibration were performed with subsequently shorter time intervals during the hybrid mapping of J0141-5427. However, only the best-behaving, least noisy antennas were used in the self-calibration processes. Thus, HH and CD were kept fixed for the 1.7-GHz observation. In the case of the 8.5-GHz observation, originally all antennas were used in phase self-calibration (except for HH which was not used in the hybrid mapping), but for the shortest time intervals, and in the amplitude self-calibration, only ATCA, MP, CD, and PA were included, while the gains of the remaining antennas were kept fixed.

### 3. Results

At both frequencies, a single radio-emitting feature was detected (Figures 1 and 2).

We derived the coordinates of the brightest pixel at both frequencies using the AIPS verb MAXFIT. At 8.5 GHz, the right ascension and declination are  $\text{RA} = 1^{\text{h}}41^{\text{m}}32.44937^{\text{s}}$  and  $\text{Dec} = -54^{\circ}27'49.9705''$ , respectively. We estimate that these coordinates are accurate within 0.8 mas. The most dominant sources of the

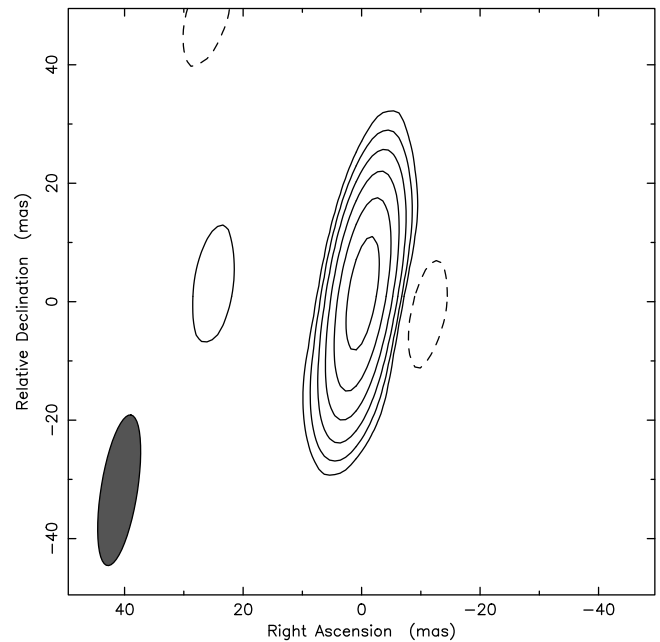


**Figure 1.** 1.7-GHz naturally-weighted LBA map of the fringe-fitted data of J0141-5427. The peak intensity is  $76.7 \text{ mJy beam}^{-1}$ . The lowest contours are at  $\pm 1.7 \text{ mJy beam}^{-1}$ , corresponding to  $4\sigma$  image noise level. Further positive contours increase by a factor of 2. The elliptical Gaussian restoring beam size is  $25.7 \text{ mas} \times 6.2 \text{ mas}$  at a major axis position angle of  $-8.9^\circ$ , and it is shown in the lower left corner of the image.

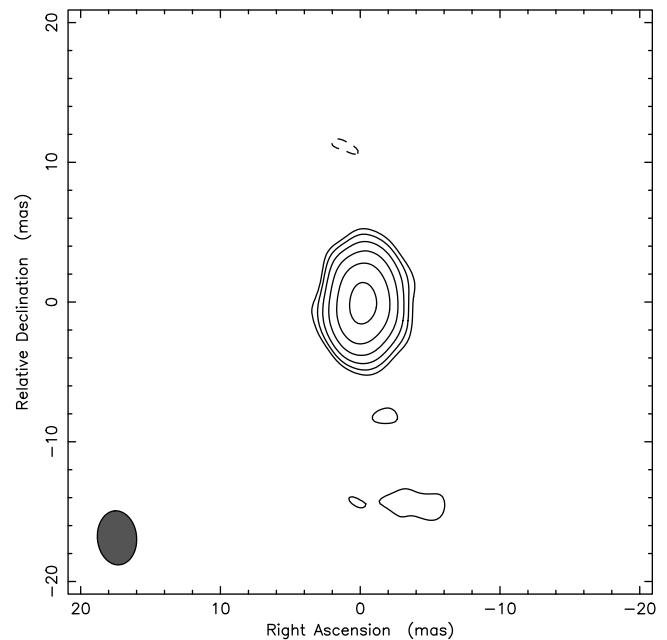


**Figure 2.** 8.5-GHz naturally-weighted phase-referenced LBA map of J0141-5427. The peak intensity is  $28.5 \text{ mJy beam}^{-1}$ . The lowest contours are at  $\pm 0.7 \text{ mJy beam}^{-1}$ , corresponding to  $4\sigma$  image noise level. Further positive contours increase by a factor of 2. The elliptical Gaussian restoring beam size is  $3.9 \text{ mas} \times 2.8 \text{ mas}$  at a major axis position angle of  $5.3^\circ$ , and it is shown in the lower left corner of the image.

uncertainty are the positional accuracy of the phase-reference calibrator (0.37 mas in right ascension and 0.33 mas in declination direction, according to the most recent version of the

Radio Fundamental Catalog<sup>c</sup>) and the astrometric errors strongly depending on the phase-reference calibrator–target angular separation. For the latter, we conservatively assumed the value derived for observations taken at 5 GHz by Chatterjee *et al.* (2004). The coordinates derived from the phase-referenced 1.7-GHz observation agree with the 8.5-GHz values within the uncertainties. Additionally, they agree within the uncertainty with the optical position provided in the Dark Energy Survey 2nd data release (Abbott *et al.* 2021). These newly derived radio coordinates of J0141–5427 are much more accurate than those previously obtained from lower-resolution radio observations, for example, the AT20 survey with  $\sim 1''$  positional accuracy (Murphy *et al.* 2010).

To quantitatively describe the brightness distribution of the source, we fitted the visibility data with Gaussian model components. At 1.7 GHz, a single circular Gaussian component with a flux density of  $(80.3 \pm 8.4)$  mJy and a full-width at half-maximum (FWHM) size of  $\sim 2.2$  mas can adequately describe the data. However, according to Lister *et al.* (2021), the typical uncertainty of a single isolated Gaussian brightness distribution component diameter is 20% of the restoring beam FWHM size. As such, the size of the component is not well-constrained. The highly elongated restoring beam of the 1.7-GHz experiment, major axis 25.7 mas in roughly north–south direction and minor axis 6.2 mas in the perpendicular direction, would result in an asymmetric source size uncertainty in the two perpendicular orientations. In the finer resolution east–west direction, the FWHM size of the emitting feature is  $(2.2 \pm 1.5)$  mas, while it is not constrained in the perpendicular direction,  $(2.2 \pm 5.1)$  mas. Nevertheless, the compactness of the radio emission is further supported by the high percentage of fringe solutions found on the longest baselines to HH.

At 8.5 GHz, an elliptical Gaussian component with a flux density of  $(40.8 \pm 4.1)$  mJy, a major and a minor axis FWHM sizes of  $(3.1 \pm 0.8)$  mas and  $(1.4 \pm 0.6)$  mas, respectively, and a major axis position angle of  $-13.7^\circ$  was needed to fit the data.<sup>d</sup> The 8.5-GHz observation is somewhat affected by time smearing effect as described in Section 2. While the peak intensity reduction of a point source may not be significant, time-average smearing can cause distortion of the image. Therefore, we also analysed the data set by excluding the longer baselines where the smearing effect is expected to be more pronounced. We only retained the antennas of MP, PA, ATCA, HO, and CD. We obtained the same parameters within the errors for the fitted Gaussian brightness distribution model, suggesting that the modelling results are robust.

Assuming the same amount of coherence loss we seen at 1.7 GHz ( $\sim 15\%$ ), the flux density of the detected feature is  $(46.9 \pm 4.7)$  mJy at 8.5 GHz.

## 4. Discussion

### 4.1. Brightness temperature

The brightness temperature of the source in the rest frame of the source can be calculated with the following equation (e.g., Veres *et al.* 2010; Hovatta *et al.* 2014):

$$T_b = 1.22 \times 10^{12} \frac{S}{\theta_{\text{maj}} \theta_{\text{min}} \nu_0^2} (1+z), \quad (1)$$

<sup>c</sup>rfc\_2022b, [http://astrogeo.org/sol/rfc/rfc\\_2022b/rfc\\_2022b\\_cat.txt](http://astrogeo.org/sol/rfc/rfc_2022b/rfc_2022b_cat.txt) (accessed 2022.09.06).

<sup>d</sup>Position angles are measured from north through east.

where  $S$  is the flux density in units of Jy,  $\nu_0$  is the observing frequency in unit of GHz, and  $\theta_{\text{maj}}$  and  $\theta_{\text{min}}$  are the major and minor axes (FWHM) of the Gaussian radio-emitting feature in units of mas. The brightness temperature of the modelled feature measured at an observing frequency of 8.5 GHz is  $T_{b, \nu_0=8.5} = (1.1 \pm 0.9) \times 10^9$  K. At 1.7 GHz observing frequency, due to the poorly constrained component size, the brightness temperature has much larger error,  $T_{b, \nu_0=1.7} = (4.2 \pm 3.1) \times 10^{10}$  K. Despite the large uncertainty,  $T_{b, \nu_0=1.7}$  exceeds  $T_{b, \nu_0=8.5}$ , which would contradict the naive expectations of detecting more compact, thus of higher brightness temperature, emitting feature in higher-resolution VLBI observation.

However, the 8.5 and 1.7 GHz observing frequencies correspond to  $\sim 51.0$  and  $\sim 10.2$  GHz rest-frame frequencies, respectively, at the redshift of the source ( $z = 5$ ). Cheng *et al.* (2020) studied a large sample (more than 800 objects) of compact, bright radio-loud AGN (mostly blazars), and showed that  $T_b$  at 43 GHz and at 86 GHz rest-frame frequencies are below the values obtained at lower rest-frame frequencies, between 2 and 22 GHz, due to synchrotron opacity effect.

By analysing data from large multi-frequency VLBI surveys, Cheng *et al.* (2020) found that the frequency-dependence of the core brightness temperature can be well described with a broken power law (up until 240 GHz), with the maximum brightness temperature reached at the break frequency of  $\sim 6.8$  GHz. Using their best fit parameters for the shape of the curve, we obtain a brightness temperature value of  $(6.4 \pm 2.0) \times 10^{10}$  K at the break frequency of 6.8 GHz (rest frame, corresponding to 1.1 GHz observing frequency). If, instead, we fit for both the break frequency,  $\nu_j$  and the brightness temperature at  $\nu_j$ , we obtain  $(20.5 \pm 8.2) \times 10^{10}$  K at a rest-frame frequency  $\nu_j = (3.6 \pm 0.4)$  GHz (corresponding to an observing frequency of 0.6 GHz).

The brightness temperature values of J0141–5427 obtained at rest-frame frequencies of 51 and 10.7 GHz clearly indicate that the radio emission is related to the activity of the central supermassive black hole in an AGN, and cannot be explained by star formation in the host galaxy (Condon 1992). At face value, they do not exceed the theoretical equipartition limit of  $\sim 5 \times 10^{10}$  K of Readhead (1994) and the empirically found median intrinsic brightness temperature of blazar sources,  $4.1 \times 10^{10}$  K (Homan *et al.* 2021). Thus, Doppler boosting is not crucially needed to explain the brightness temperature values, however it cannot be ruled out. On the other hand, taking the decrease in brightness temperature at high rest-frame frequencies well above the break frequency into account, the measured brightness temperatures are compatible with those of a slightly Doppler boosted blazar source.

Brightness temperature values significantly below the equipartition limit usually correspond to physical processes in evolved plasma regions and not in the compact regions of blazar jets. However, such low brightness temperatures can also be measured in blazars due to insufficient resolution, when the core and a close jet component cannot be resolved and thus the fitted size is larger, resulting in lower  $T_b$  value. Hovatta *et al.* (2014) studied 190 blazar jets of the Monitoring Of Jets in Active galactic nuclei with VLBA Experiments (MOJAVE, Lister *et al.* 2019) survey, and showed that in sources at higher redshifts<sup>e</sup> the derived core parameters are more likely contaminated by a neighbouring jet component due to the lower effective linear resolution.

<sup>e</sup>The highest-redshift objects of this sample are at  $z \approx 3.3$  (Hovatta *et al.* 2014).

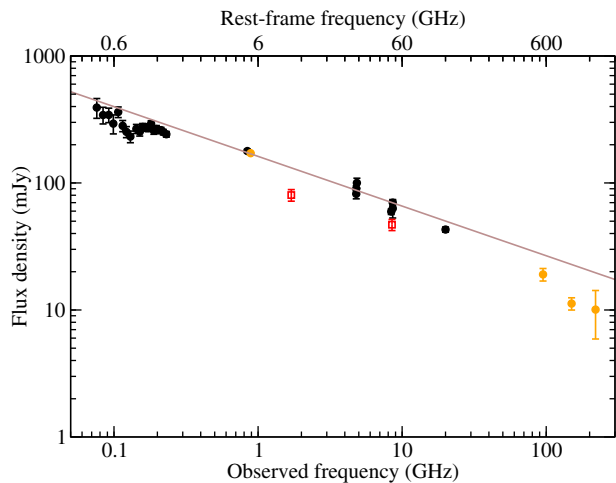


**Figure 3.** Radio spectrum of J0141-5427. Black circles are low-resolution archival measurements (for references, see Belladitta et al. 2019). Orange circles are from the RACS DR1 (McConnell et al. 2020; Hale et al. 2021), and from the SPT-SZ survey (Everett et al. 2020). Red squares are our LBA flux densities. The brown line represents a power law fit to the low-resolution data (black and orange symbols).

Interestingly, high brightness temperature values, close to the equipartition limit are rarely observed in other  $z > 5$  blazars (Coppejans et al. 2016; Zhang et al. 2022), with the notable exception of J0906+6930 (An et al. 2020).

#### 4.2. Flux density and spectral index

Compared to lower-resolution radio observations of J0141-5427, there is a significant difference in the recovered flux density. According to the AT20G survey, the source had a flux density of  $(70.0 \pm 4.0)$  mJy at 8.6 GHz, measured between 2004 and 2008 with the ATCA (Chhetri et al. 2013). This discrepancy can be due to resolution effect, that is, the LBA observation resolving out a significant fraction of extended radio emission, and/or source flux density variability in time.

We can derive the spectral index ( $\alpha$ ) of the compact radio-emitting feature between 1.7 and 8.5 GHz observing frequencies using the flux densities obtained from the Gaussian model fitting to our LBA visibility data. The spectral index is defined as  $S \propto \nu^\alpha$ . For J0141-5427,  $\alpha = -0.33 \pm 0.13$ , thus it has a flat radio spectrum. This is a typical spectral index value for the core of jetted AGN (e.g., Hovatta et al. 2014) between 8 and 15 GHz.

The source shows a similarly flat radio spectrum between 76 MHz and 20 GHz in archival low-resolution radio observations as reported by Belladitta et al. (2019). Since that publication, the first data release of the Australian Square Kilometre Array (SKA) Pathfinder (ASKAP), the Rapid ASKAP Continuum Survey (RACS, McConnell et al. 2020; Hale et al. 2021) has become public. In addition, we included high-frequency radio flux density measurements obtained with the South Pole Telescope (SPT) within the framework of SPT Sunyaev-Zeldovich survey (SPT-SZ, Everett et al. 2020). The most complete radio spectrum of J0141-5427 is shown in Figure 3.

J0141-5427 has been detected in RACS as a single-component source with a flux density of  $(174.0 \pm 13.0)$  mJy at 888 MHz (Figure 4). This value agrees within the errors with the closest-frequency measurements taken at 843 MHz by the Sydney University Molonglo Survey (SUMSS, Mauch et al. 2003) in 2002.

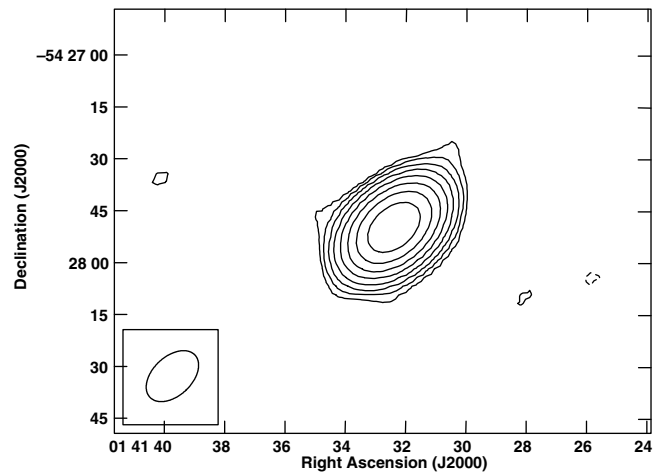


**Figure 4.** ASKAP image of J0141-5427 at 888 MHz from RACS (McConnell et al. 2020; Hale et al. 2021). Peak brightness is  $162.6 \text{ mJy beam}^{-1}$ . The lowest contours are drawn at  $\pm 0.68 \text{ mJy beam}^{-1}$  corresponding to an image noise level of  $3\sigma$ , further positive contour levels increase by a factor of two. The restoring beam is  $17.84'' \times 11.28''$  at a major axis position angle of  $-46.7^\circ$ , as shown in the lower left corner of the image.

At higher frequencies, J0141-5427 was detected in all three bands of the SPT-SZ, at 95, 150, and 220 GHz (however, at the highest frequency only with a signal-to-noise ratio of 2.9) with flux densities of  $S_{95} = (19.1 \pm 2.2)$  mJy,  $S_{150} = (11.2 \pm 1.2)$  mJy, and  $S_{220} = (10.1 \pm 4.2)$  mJy, respectively. These measurements indicate a possible steepening of the radio spectrum at high frequencies. However, the broad-band radio spectrum is still flat with  $\alpha_{0.076}^{220} = -0.39 \pm 0.02$ . The observing frequencies of SPT correspond to rest-frame frequencies of 570, 900, and 1320 GHz, where the emission from the dust in the host galaxy may have a growing contribution to the measured flux density (Planck Collaboration et al. 2016; Massardi et al. 2022).

There is no sign of spectral turnover of the radio spectrum at observed frequencies around 0.6 and 1.0 GHz corresponding to the rest-frame turnover values estimated from the brightness temperatures (see Section 4.1). There is a hint of spectral flattening at around a few hundred MHz measured by the GaLactic and Extragalactic All-Sky MWA Survey (GLEAM) (Belladitta et al. 2019), which is followed by a steepening at lower observed frequencies, below  $\sim 130$  MHz. However, this apparent rise of the flux density with decreasing frequency (and thus decreasing angular resolution) could be caused by source confusion; according to Franzen et al. (2019), confusion is the limiting noise factor at  $\lesssim 100$  MHz in the GLEAM data. The effect of confusion, the target source being blended with its neighbours, has also been seen in lower frequency GLEAM data by An et al. (2022, submitted).

#### 4.3. Magnetic field strength

The magnetic field strength of a compact synchrotron self-absorbed source can be estimated if the frequency of the spectral turnover from the optically thick to the optically thin region, and the flux density ( $S_j$ ) and the angular size of the emitting region at the turnover point ( $\theta_j$ ) are known (Marscher 1983),

$$B = 10^{-5} b(\alpha) \theta_j^4 v_j^5 S_j^{-2} \frac{\delta}{1+z}, \quad (2)$$

where  $\delta$  is the relativistic Doppler boosting factor, and  $b(\alpha)$  is a numerical factor depending on the spectral index tabulated in Marscher (1983).

Using  $\nu_j = 6.8$  GHz from Cheng et al. (2020) and assuming that  $\alpha$  does not change till the turnover, we can calculate the expected flux density at this (rest-frame) frequency,  $S_j = 92.1$  mJy. The size of the emitting region can be derived from the fitted brightness temperature as  $\theta_j = 3.0$  mas. Thus, the magnetic field strength can be given as  $B = 1.6\delta$  G. Alternatively, using the fitted turnover (rest-frame) frequency value of,  $\nu_j = 3.6$  GHz, one can obtain a much lower magnetic field strength of  $B = 0.083\delta$  G.

Since there is no indication of substantial relativistic boosting in the source, the Doppler factor is expected to have a value below 10, the above estimated magnetic field strength remains well below the one obtained by Belladitta et al. (2019),  $B \approx 9$  G. However, the value derived by Belladitta et al. (2019) characterises the magnetic field strength at close proximity (fraction of a parsec) to the black hole, while the one estimated from the radio jet is much farther away from the central engine.

Additionally, the above calculation of the magnetic field strength relies on the brightness temperature and size estimations, which may only be limiting values (upper limit on the actual source size, thus lower limit on the brightness temperature) due to the resolution. Therefore, this can also hinder the comparison of the magnetic field strength derived from the X-ray observations and from radio data.

#### 4.4. Radio power

We can use the derived spectral index and flux densities to calculate the monochromatic radio powers (Hogg et al. 2002):

$$P_\nu = 4\pi D_L^2 S_\nu (1+z)^{-\alpha-1} \quad (3)$$

The obtained radio power values are  $P_{1.7} = (7.9 \pm 0.8) \times 10^{27}$  W Hz<sup>-1</sup> and  $P_{8.5} = (4.6 \pm 1.4) \times 10^{27}$  W Hz<sup>-1</sup>. Compared to other high-redshift radio-loud AGN, J0141–5427 is among the most powerful ones in the radio regime (Coppejans et al. 2016; Sotnikova et al. 2021; Krezinger et al. 2022).

#### 4.5. J0141–5427 as a potential VLBI reference source

The sky density of known compact bright extragalactic radio sources suitable as VLBI calibrators at declinations below about  $-40^\circ$  is significantly lower than at higher declinations (e.g., Charlot et al. 2020). This is because most VLBI networks operate on the northern hemisphere. While J0141–5427 with its 8.5-GHz flux density of  $\sim 47$  mJy (Section 3) is not bright enough for the inclusion in the regular geodetic VLBI observational programmes (e.g., Plank et al. 2017), it may serve as a phase-reference source for observing weaker nearby targets for high-resolution imaging or relative astrometric positioning. This is especially true at lower frequencies, as indicated by the high rate of fringe-fit solutions found for J0141–5427 in our experiment at 1.7 GHz. So far, VLBI imaging surveys of low-declination southern radio AGN have mainly concentrated on bright sources with at least  $\sim 100$  mJy flux densities (e.g., Shen et al. 1997, 1998; Ojha et al. 2004, 2005, 2010; Müller et al. 2018).

#### 5. Other X-ray weak blazar candidates

Since J0141–5427 is the only known blazar candidate at high redshift with an intense radio but with a very weak X-ray emission,

Belladitta et al. (2019) searched for similar X-ray weak radio-bright blazar candidates in the local Universe using the 5th edition of the Roma-BZCAT multi-frequency catalogue of blazars (Massaro et al. 2009). They selected flat-spectrum radio sources with flux densities measured at 1.4 GHz or 843 MHz exceeding 1.5 Jy. All these sources have X-ray detections. The authors focused only on sources with 1.4-GHz radio power similar to that of J0141–5427. They found only two objects (2 % of their sample) with as low X-ray-to-radio luminosity ratio as for J0141–5427.

5BZQ J2206–1835 is a quasar at redshift  $z = 0.619$  (Morton & Tritton 1982). It was observed in the prelaunch survey of the VLBI Space Observatory Programme by Fomalont et al. (2000) at 5 GHz. It was detected only at the shortest baselines of the Very Long Baseline Array (VLBA). In a 22 GHz VLBA survey, Moellenbrock et al. (1996) did not detect the source. Thus these high-resolution observations did not confirm the blazar nature of 5BZQ J2206–1835, as they failed to reveal any bright compact radio-emitting feature at mas scale.

5BZQ J2038+5119, also known as 3C 418, is a quasar at a redshift of  $z = 1.686$  (Spinrad et al. 1985). It was observed within the framework of the MOJAVE (Lister et al. 2019) survey at 15 GHz. It has a one-sided jet structure with apparent superluminal motion exceeding  $6c$  (Lister et al. 2019). The brightness temperature of the core component is between  $4.6 \times 10^{11}$  K and  $5.2 \times 10^{12}$  K (according to the brightness distribution model of the jet obtained given in Lister et al. 2019), thus it exceeds the equipartition limit and implies Doppler boosting. The object was also detected in  $\gamma$ -rays by the Large Area Telescope onboard the *Fermi* satellite (Abdollahi et al. 2020).

Thus, the three similarly weak at X-ray radio-loud AGN exhibit very different radio characteristics, forming a heterogeneous group. One of them is a genuine relativistically boosted blazar, another one is not a blazar according to its VLBI observations, and J0141–5427 has a modest measured brightness temperature, however, it is compact enough to be detected on intercontinental radio interferometric baselines.

#### 6. Summary

Belladitta et al. (2019) reported the discovery of a radio-loud AGN at a redshift of  $z = 5$ , which they identified as a possible blazar. Contrary to the expectations, the X-ray emission of this source, J0141–5427, is very weak.

We performed mas-scale resolution radio imaging observations of J0141–5427 using the Australian LBA at 1.7 and 8.5 GHz. We detected a single bright, compact feature at both frequencies. This and the flat radio spectrum of the mas-scale feature strengthen its blazar classification. The estimated brightness temperature values clearly indicate the AGN origin of the radio emission.

The relatively low brightness temperature value measured at the rest-frame frequency of  $\sim 50$  GHz is in accordance with the findings of Cheng et al. (2020). Thus, it still allows for moderate relativistic Doppler boosting that could be directly observable at a lower frequency, in support of the blazar nature of the source. High-resolution VLBI imaging at observed frequencies below 1 GHz can sample the assumed turn-over region in the brightness temperature values and provide a Doppler factor for J0141–5427. However, such low-frequency ( $\lesssim 1$  GHz), high-resolution observations are currently not achievable.

We investigated the radio properties of two other blazar candidates which have similarly low X-ray-to-radio luminosity ratios as J0141–5427. We found that while one of them (J2038+5119) clearly shows relativistically boosted radio emission, the other one (J2206–1835) is certainly not a blazar.

J0141–5427 was detected in X-ray so far in only one observation in 2005, while remained undetected in 2018 (Belladitta et al. 2019). Since blazars are known to show significant variability, a new X-ray observation may provide a better constraint on the high-energy properties of this source.

**Acknowledgement.** We thank the referee for his useful feedback that have improved this manuscript. The Long Baseline Array is part of the Australia Telescope National Facility (<https://ror.org/05qajvd42>, accessed 2022.09.10) which is funded by the Australian Government for operation as a National Facility managed by CSIRO. This work was supported by resources provided by the Pawsey Supercomputing Centre with funding from the Australian Government and the Government of Western Australia. The ASKAP radio telescope is part of the Australia Telescope National Facility which is managed by Australia's national science agency, CSIRO. Operation of ASKAP is funded by the Australian Government with support from the National Collaborative Research Infrastructure Strategy. ASKAP uses the resources of the Pawsey Supercomputing Research Centre. Establishment of ASKAP, the Murchison Radio-astronomy Observatory and the Pawsey Supercomputing Research Centre are initiatives of the Australian Government, with support from the Government of Western Australia and the Science and Industry Endowment Fund. We acknowledge the Wajarri Yamatji people as the traditional owners of the Observatory site. This paper includes archived data obtained through the CSIRO ASKAP Science Data Archive, CASDA (<https://data.csiro.au>). LIG acknowledges support by the CSIRO Distinguished Visitor Programme. HC acknowledges support from the Hebei Natural Science Foundation of China (Grant No. A2022408002), and the National Natural Science Foundation of China (Grants No. U2031116 and U1731103). This research was supported by the Australian Research Council Centre of Excellence for All-Sky Astrophysics in three Dimensions (ASTRO-3D), through project number CE170100013. KR acknowledges support from the Bundesministerium für Bildung und Forschung (BMBF) award 05A20WM4. This research was supported by the Hungarian National Research, Development and Innovation Office (NKFIH), grant number OTKA K134213.

## References

- Abbott, T. M. C., et al. 2021, *ApJS*, **255**, 20
- Abdollahi, S., et al. 2020, *ApJS*, **247**, 33
- An, T., et al. 2020, *NatC*, **11**, 143
- Beasley, A. J., & Conway, J. E. 1995, in *Astronomical Society of the Pacific Conference Series*, Vol. 82, *Very Long Baseline Interferometry and the VLBA*, ed. J. A. Zensus, P. J. Diamond, & P. J. Napier, 327
- Belladitta, S., et al. 2019, *A&A*, **629**, A68
- Bridle, A. H., & Schwab, F. R. 1999, in *Astronomical Society of the Pacific Conference Series*, Vol. 180, *Synthesis Imaging in Radio Astronomy II*, ed. G. B. Taylor, C. L. Carilli, & R. A. Perley, 371
- Charlot, P., et al. 2020, *A&A*, **644**, A159
- Chatterjee, S., et al. 2004, *ApJ*, **604**, 339
- Cheng, X. P., et al. 2020, *ApJS*, **247**, 57
- Chhetri, R., Ekers, R. D., Jones, P. A., & Ricci, R. 2013, *MNRAS*, **434**, 956
- Condon, J. J. 1992, *ARA&A*, **30**, 575
- Coppejans, R., et al. 2016, *MNRAS*, **463**, 3260
- Deller, A. T., et al. 2011, *PASP*, **123**, 275
- Everett, W. B., et al. 2020, *ApJ*, **900**, 55
- Fomalont, E. B., et al. 2000, *ApJS*, **131**, 95
- Franzen, T. M. O., et al. 2019, *PASA*, **36**, e004
- Greisen, E. W. 1990, in *Acquisition, Processing and Archiving of Astronomical Images*, 125
- Gurvits, L. I., Frey, S., & Paragi, Z. 2015, in *Extragalactic Jets from Every Angle*, ed. F. Massaro, C. C. Cheung, E. Lopez, & A. Siemiginowska (Vol. 313), 327
- Hale, C. L., et al. 2021, *PASA*, **38**, e058
- Högbom, J. A. 1974, *A&AS*, **15**, 417
- Hogg, D. W., Baldry, I. K., Blanton, M. R., & Eisenstein, D. J. 2002, arXiv e-prints, astro
- Homan, D. C., et al. 2021, *ApJ*, **923**, 67
- Hovatta, T., et al. 2014, *AJ*, **147**, 143
- Ivezić, et al. 2002, *AJ*, **124**, 2364
- Kellermann, K. I., & Pauliny-Toth, I. I. K. 1969, *ApJL*, **155**, L71
- Kreuzer, M., et al. 2022, *ApJS*, **260**, 49
- Lister, M. L., et al. 2021, *ApJ*, **923**, 30
- Lister, M. L., et al. 2019, *ApJ*, **874**, 43
- Marscher, A. P. 1983, *ApJ*, **264**, 296
- Martí-Vidal, I., et al. 2010, *A&A*, **515**, A53
- Massardi, M., et al. 2022, *MNRAS*, **513**, 6013
- Massaro, E., et al. 2009, *A&A*, **495**, 691
- Mauch, T., et al. 2003, *MNRAS*, **342**, 1117
- McConnell, D., et al. 2020, *PASA*, **37**, e048
- Moellenbrock, G. A., et al. 1996, *AJ*, **111**, 2174
- Morton, D. C., & Tritton, K. P. 1982, *MNRAS*, **198**, 669
- Müller, C., et al. 2018, *A&A*, **610**, A1
- Murphy, T., et al. 2010, *MNRAS*, **402**, 2403
- Ojha, R., et al. 2004, *AJ*, **127**, 3609
- Ojha, R., et al. 2005, *AJ*, **130**, 2529
- Ojha, R., et al. 2010, *A&A*, **519**, A45
- Planck Collaboration, et al. 2016, *A&A*, **594**, A26
- Plank, L., et al. 2017, *JG*, **91**, 803
- Readhead, A. C. S. 1994, *ApJ*, **426**, 51
- Shen, Z. Q., et al. 1997, *AJ*, **114**, 1999
- Shen, Z. Q., et al. 1998, *AJ*, **115**, 1357
- Shepherd, M. C. 1997, in *Astronomical Society of the Pacific Conference Series*, Vol. 125, *Astronomical Data Analysis Software and Systems VI*, ed. G. Hunt & H. Payne, 77
- Sotnikova, Y., et al. 2021, *MNRAS*, **508**, 2798
- Spinrad, H., Djorgovski, S., Marr, J., & Aguilar, L. 1985, *PASP*, **97**, 932
- Urry, C. M., & Padovani, P. 1995, *PASP*, **107**, 803
- Veres, P., Frey, S., Paragi, Z., & Gurvits, L. I. 2010, *A&A*, **521**, A6
- Wright, E. L. 2006, *PASP*, **118**, 1711
- Wrobel, J. M. 1995, in *Astronomical Society of the Pacific Conference Series*, Vol. 82, *Very Long Baseline Interferometry and the VLBA*, ed. J. A. Zensus, P. J. Diamond, & P. J. Napier, 411
- Zhang, Y., et al. 2022, *A&A*, **662**, L2